PAPER

Check for updates

Gemological characteristics and inclusions of green rutilated quartz from Huanggangliang, Inner Mongolia

ShuXin Zhao,[a] Tao Li,[a] Qingfeng Guo, [iD] *[a] LiangYu Liu,[a] Yinghua Rao[a] and Libing Liao [iD] *[b]

Normally, various minerals exist in quartz as inclusions. In this study, methods such as gem microscopy, polarizing microscopy, Fourier transform infrared (FTIR) spectroscopy, Raman spectroscopy, and electron probe microanalysis (EPMA) were used to systematically study the gemological characteristics and inclusions in green rutilated quartz from Inner Mongolia. Results show that the sample appears green due to the chaotic distribution of green inclusions in the shape of hair filaments. Combined with the chemical composition, the inclusions are Ca–Fe-rich amphiboles with compositions very close to those of the end-member ferro-actinolite. According to the principle of amphibole nomenclature, the inclusions are named ferro-actinolite in the subclass of calc-alkaline amphiboles with a few named ferro-hornblende. Results suggested that the inclusions in green rutilated quartz were formed during the late stage of quartz crystallization. This work provides a new theoretical basis for the study of green rutilated quartz in Huanggangliang, Inner Mongolia.

1 Introduction

Quartz is one of the most common minerals in the world and is popular for its good transparency and beautiful appearance. Because quartz is widely circulated in the market, research on inclusions in quartz crystals has attracted considerable attention.[1–3] Quartz has different genesis types and is mainly formed in pegmatite deposits, skarn deposits and hydrothermal deposits.[4] The formation of quartz deposits in skarn is largely related to the hydrothermal magmatic fluids in granite. Skarn is brittle and easily fractured, and it is easy for cracks to form under the action of tectonic stress. In the late stage of quartz sulfide mineralization, aplite is mostly filled in veins along cracks to replace skarn minerals formed in the early stage or those occurring in crystal holes and then crystallize and grow in a certain space in the form of crystal clusters.[5] The common solid inclusions in quartz mainly include rutile, actinolite, chlorite, hematite, and pyrite.[6–8] When the solid inclusions in quartz are in the form of fibers and hairline, they are called rutilated quartz; the common ones are rutilated quartz (rutile), black rutilated quartz (tourmaline), and green rutilated quartz (actinolite).[9–12]

The color of quartz may be attributed to electronic defects in the crystal structure or to other elements doped into the crystal structure.[13] As for the cause of green quartz coloration, previous research suggests that the color of green rutilated quartz is related to Fe^{2+} or Fe^{3+}.[14–16] In addition, some small (usually nanoscale) well-dispersed mineral inclusions can affect the color formation of quartz and other minerals.[17] In later studies, it was found that green rutilated quartz appears green due to the presence of dense green amphibole inclusions. Maneta *et al.* suggested that the green color of quartz is caused by nanometer to micrometer-sized actinolite inclusions.[8,13] Jiang *et al.* found trapiche-like quartz in Inner Mongolia. The fibrous inclusions were identified as ferro-actinolite from EPMA and Raman spectroscopy.[18] In summary, green rutilated quartz from different regions may have different types of amphibole inclusions. Therefore, it is necessary to discuss the gemological and mineralogical characteristics as well as the color genesis of green rutilated quartz from Inner Mongolia.

Currently, the research on green rutilated quartz is mainly focused on the morphological features, identification characteristics, growth environment and other aspects. There are few studies on the gemological characteristics of green rutilated quartz from Inner Mongolia and their inclusions. In this study, the green rutilated quartz collected from Huanggangliang, Inner Mongolia served as the research object. Traditional gemological testing methods were applied to analyze the gemological and appearance characteristics of the samples. Fourier transform infrared (FTIR) spectroscopy, Raman spectroscopy and electron probe microanalysis (EPMA) were used to

[a]School of Gemmology, China University of Geosciences, Beijing, 100083, China. E-mail: qfguo@cugb.edu.cn

[b]Beijing Key Laboratory of Materials Utilization of Nonmetallic Minerals and Solid Wastes, National Laboratory of Mineral Materials, School of Materials Sciences and Technology, China University of Geosciences, Beijing 100083, China. E-mail: clayl@cugb.edu.cn

study the spectral characteristics and discuss the composition and morphology of the inclusions in green rutilated quartz. The results provide new mineral information on quartz growth and enrich the gemological and spectroscopic features of green rutilated quartz from Inner Mongolia. Finally, based on the experimental information, the mineralization environment of green rutilated quartz was inferred.

2   Materials and methods

2.1.   Materials

Five samples (Fig. 1b) were mined from Huanggangliang Iron Ore VI Mine, Hexigten Banner, Inner Mongolia, which were labeled as MGC-1 to 5. Samples ranged from 4 to 6 cm in length and 2 to 3 cm in width. The mine is located in eastern Inner Mongolia, at the southern and western ends of the Great Xing'an Range mineralized belt, as shown in Fig. 1a.[19,20] The non-metallic minerals in the Huanggangliang deposit are very complex. There are more than 40 types of rock-forming minerals in various dry and wet skarn minerals and medium-basic magmatic rocks, which reflect the complex mineralization evolution history of the mining area.

The samples showed a dark green appearance and were more heavily weathered; all samples were covered with a yellow-weathered layer.

2.2.   Methods

Standard gemological properties of the samples were determined, including refractive index, specific gravity, and microscopic features. Microscopic observation was completed using GI-MP22 gemological photographic microscopy and polarizing microscopy (BX51).

Infrared spectroscopy was performed using the reflection method by polishing the samples to ensure a smooth surface. Infrared spectra were obtained using the FT-IR Spectrometer Tensor 27 (Bruker, Germany) at the Gem Testing Laboratory at the School of Gemmology, China University of Geosciences, Beijing. The scanning range was 100–4000 cm^{-1}. The resolution

was 4 cm^{-1} and the number of scans was 50–100. The power frequency was between 47 and 65 Hz and the voltage used in the experiment was 85–265 V.

Raman spectra were collected on the HR Evolution Micro-Raman spectroscope (HORIBA, Japan) at the Gem Testing Laboratory at the School of Gemmology, China University of Geosciences, Beijing. Experimental test conditions were as follows: the excitation light source was 532 nm, grating was 600 (500 nm), test range was between 100 and 4000 cm^{-1}, integration time was 3 s, laser power was 30–40 mW, experimental voltage was 220 V, and current was 10 A.

EMPA data were collected using EPMA-1600 (Shimadzu, Japan) at the Geoscience Test Center of China University of Geosciences, Beijing. The test conditions were as follows: acceleration voltage was 15 kV, current was 10 nA, electron beam spot diameter was 5 μm, and carbon was sprayed on the sample surface.

3   Results and discussion

3.1.   Gemological properties

The main body of the sample was dark green with generally poor transparency. The surface of the sample was severely exfoliated with no fixed crystal shape. The specific gravity of the whole sample was 2.59–2.6. Green quartz with better crystal shapes can be barely seen as hexagonal columns and hexagonal monoclinic cones.

MGC-4 had a good hexagonal columnar shape, and the crystal surface can be seen as sparkling small crystal surfaces (Fig. 2a). Under a microscope, some of the samples had a more disorganized crystal surface in MGC-3 (Fig. 2b). After polishing their surfaces, the intense fibrous and acicular inclusions could be seen inside. The length of the inclusions ranged from 10 to 400 μm, the width ranged from 1 to 10 μm, and the color was dark green. The inclusions varied greatly in thickness and were randomly distributed in different parts of the crystals with no obvious regularity (Fig. 2c). MGC-4 was cut perpendicular to the c-axis of the crystals with parallel-oriented acicular inclusions
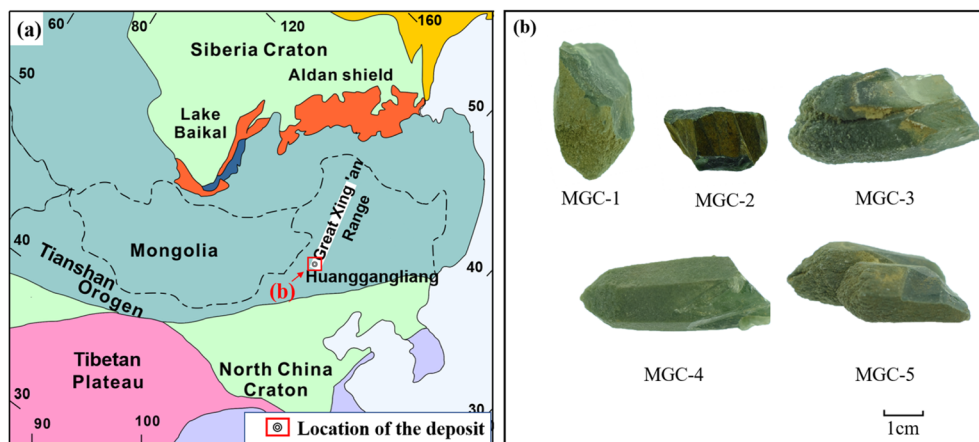

Fig. 1   (a) Geological simplified sketch map of the tectonic zoning of Northeast China (modified after Jahn et al., 2004 and Kröner et al. (2008))[19,20] (b) pictures of green rutilated quartz.
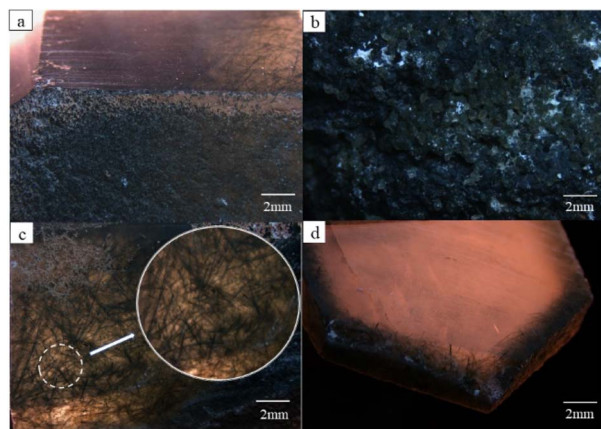
Fig. 2 Characteristics of green rutilated quartz samples under the gemological microscopy. (a) Enlarged view of column surface of MGC-4; (b) parallel consecutive crystals of MGC-3; (c) filamentous inclusions of MGC-4; (d) slices perpendicular to *c* axis of MGC-4.

intersecting the *c*-axis at an angle. The direction of inclusions growth expansion has nothing to do with the crystal axis (Fig. 2d). In conclusion, the spatial distribution of inclusions showed that there were more inclusions at the tip, fewer at the bottom, more on the surface, and fewer inside.

To clearly observe the characteristics of the internal inclusions of the green rutilated quartz, the sample sections were observed with a BX51 polarizing microscope, where a large number of cloudy liquid inclusions and brown bands were observed in MGC-4 (Fig. 3a). Note that additional magnification showed that the cloudy inclusion is composed of tiny droplets and the brown bands are fissures (Fig. 3b). Color-impregnated parallel cracks (Fig. 3c) and intersecting fibrous inclusions (Fig. 3d) could be observed in MGC-2 and MGC-5. The conditions observed using the polarizing microscope and gem microscope were basically the same. Owing to a large number of green fibrous inclusions inside, the crystal itself appears colorless green.
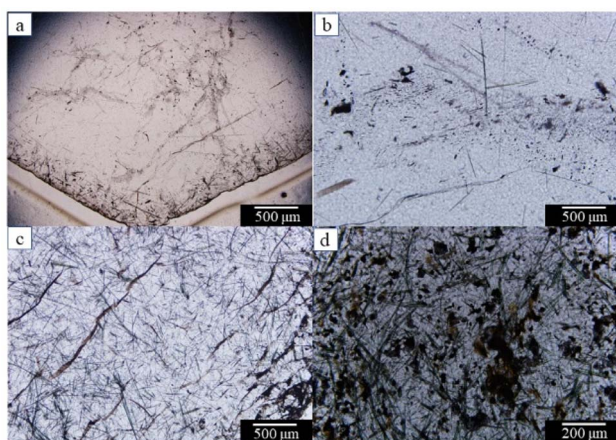
The condition of undulatory extinction is common in minerals such as quartz and feldspar in metamorphic rocks.[21] Note that undulatory extinction was observed in MGC-5 (Fig. 4), which was a banded extinction condition corresponding to the extinction pattern in the sample. It was characterized by an extinction band with a clear boundary at the twisted part when the mineral crystal was deformed by an external force. The extinction bands extended in the same direction as the bright part and appeared in regular alternation between them. This phenomenon indicates that the crystals were subjected to a large amount of stress.[22]

3.2. Infrared spectra analysis

Two samples, MGC-1 and MGC-2, which are densely packed with inclusions, were tested by the reflection method, and the results are shown in Fig. 5.

The results show that the absorption peaks of the green rutilated quartz samples are 470, 555, 694, 800, 1103, and 1160 cm^{-1}, in which the Si–O asymmetric stretching vibration bands are obvious in the range of 900–1200 cm^{-1}. The characteristic peaks of the standard quartz sample are 453, 547, 694, 779, 796, 1078, and 1162 cm^{-1} in the RRUFF database.[23] The comparison demonstrated that the green rutile quartz sample had the same spectrum as quartz. Among them, the peaks at 470 and 555 cm^{-1} belong to the Si–O bending vibration. The peak at 800 cm^{-1} belongs to the symmetric stretching vibration peak of Si–O.[24,25] The infrared beam directed toward the crystal along the *c*-axis direction produced an infrared spectrum with only one peak at 800 cm^{-1}, while the spectrum obtained along the other directions showed an additional peak at 779 cm^{-1}, which reflected the directionality of the symmetric stretching vibration of the Si–O.[26,27]

3.3. Raman spectra analysis

Fig. 6 shows the Raman spectra of five green rutilated quartz samples, which were consistent with those from card R#050025 in the RRUFF database.[23] Table 1 shows the corresponding

Fig. 3 Characteristics of green rutilated quartz samples under the polarizing microscopy: (a) cloudy inclusion of MGC-4, (b) cloudy inclusion after magnification of MGC-4, (c) fissures arranged in parallel of MGC-2, (d) intersecting fibrous inclusions of MGC-5.
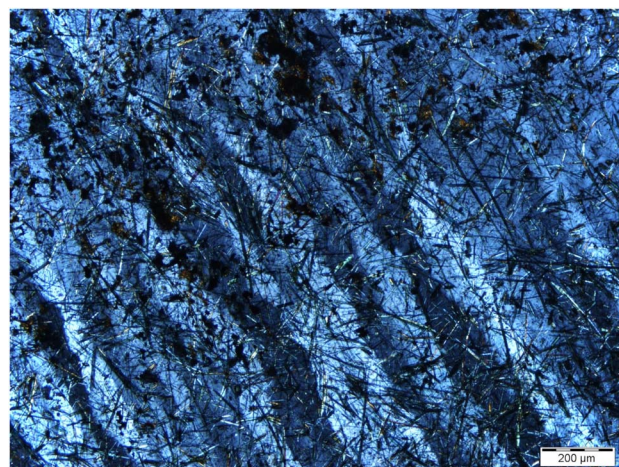

Fig. 4 Undulatory extinction phenomenon of MGC-5 under the polarizing microscope.
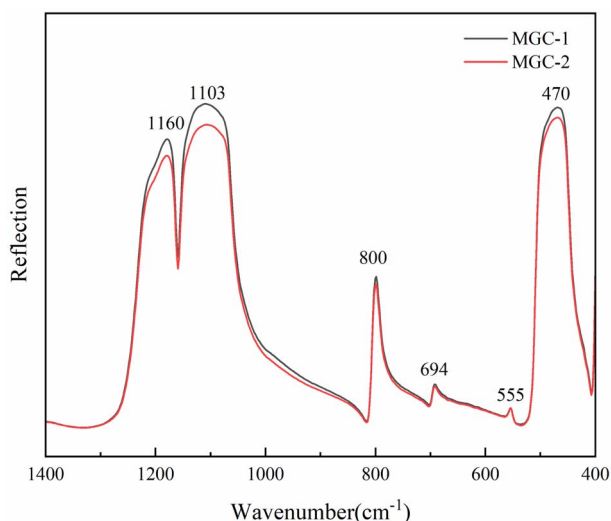
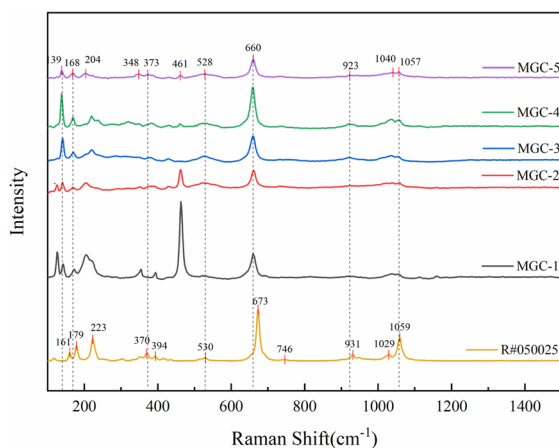Fig. 5 Infrared spectra (reflection) of green rutilated quartz samples.

Fig. 6 Raman spectra of the five samples and standard actinolite.

structures of the Raman characteristic peaks. Results indicate that the Raman spectra of the inclusions exhibit four groups of different strengths in the range of 100–1200 cm^{-1}, which are primarily caused by the vibration of the $[Si_4O_{11}]$ group. By comparing the standard actinolite Raman spectra,[28] the inclusions can be identified as actinolite.

Among them, the strongest peak at 660 cm^{-1} is attributed to Si–O–Si stretching vibration; the stronger peak at 923 cm^{-1} and the shoulder peaks at 1040 and 1057 cm^{-1} are attributed to Si–O stretching vibration. The weaker peaks at 348, 373, and

528 cm^{-1} are attributed to Si–O bending vibrations, and the strong peaks at 139, 168, and 221 cm^{-1} are attributed to lattice vibrations.[29]

The standard peaks of actinolite are located at 161, 179, 223, 370, 394, 530, 673, 746, 931, 1029, and 1059 cm^{-1}. The comparison shows that the peaks of the Raman spectra of the inclusions inside the green rutilated quartz are slightly lower than those of the standard actinolite with an approximate difference of 0–10 cm^{-1}, which is related to the differences in the chemical composition.[30]

In addition, clear gas–liquid inclusions were observed inside the green rutilated quartz under the microscope. They were analyzed by Raman spectroscopy and the results are shown in Fig. 7. Three distinct peaks in the range of 1500–4000 cm^{-1} were observed, including the H–OH bending vibration at 1642 cm^{-1}, the O–H antisymmetric stretching vibration at 3263 cm^{-1}, and the O–H symmetric stretching vibration at 3442 cm^{-1}. This is consistent with the Raman spectrum of water, indicating that the liquid in the gas–liquid inclusion is water.[31]

3.4. Chemical composition analysis of inclusion

Electron probe microanalysis (EPMA) is currently the most widely used technique for the quantitative analysis of trace elements. The lower limit of detection is typically 0.01%; the relative error of the quantitative analysis of major elements is typically less than 2%.[32] Table 2 shows the EPMA test results for the inclusions in green rutilated quartz. The results showed that the chemical components of the inclusion are mainly SiO_2,

Fig. 7 Raman spectra of partial liquid inclusions in MGC-4.

Table 1 Assignment of Raman spectra of green rutilated quartz

Raman peak (cm^{-1})	Standard actinolite (cm^{-1})[23]	Band assignment[28]
126, 139, 168, 220	127, 161, 179, 223	Lattice vibration
348, 373, 461, 528	352, 370, 530	Si–O bending vibration
660	673	Si–O–Si stretching vibrations
923, 1040, 1057	931, 1029, 1059	Si–O stretching vibrations

Table 2 EPMA data of inclusions in green rutilated quartz[a]

Name	SiO$_2$ wt%	TiO$_2$ wt%	Al$_2$O$_3$ wt%	Cr$_2$O$_3$ wt%	FeO wt%	MnO wt%	NiO wt%	MgO wt%	CaO wt%	Na$_2$O wt%	K$_2$O wt%	CoO wt%	Total wt%
MGC-5-1	46.666	0.018	5.632	0.055	29.131	1.01	0.081	2.929	11.342	0.568	0.305	0.028	97.765
MGC-5-2	49.589	0	2.879	0	29.819	1.278	0	2.407	11.149	0.318	0.292	0.085	97.816
MGC-5-3	49.128	0.039	3.245	0	27.917	1.175	0.015	3.717	11.496	0.366	0.279	0.063	97.44
MGC-5-4	48.614	0	3.769	0.002	29.514	0.593	0.003	2.627	11.211	0.489	0.462	0.051	97.336
MGC-5-5	48.582	0.064	3.135	0	29.356	1.325	0	2.814	11.386	0.431	0.333	0.139	97.566
MGC-5-6	48.706	0.007	3.845	0.063	29.344	0.861	0.037	2.415	10.71	0.52	0.242	0.048	96.8
MGC-5-7	47.26	0.016	4.847	0	29.822	0.5	0	2.95	11.459	0.642	0.381	0.036	97.914
MGC-5-8	47.942	0.018	3.15	0.007	29.492	0.74	0.035	2.693	11.345	0.452	0.403	0.029	96.305
MGC-1	47.805	0	4.399	0.066	28.731	1.021	0	2.93	11.218	0.535	0.295	0.121	97.121
MGC-2	50.427	0.074	2.117	0.002	26.932	1.028	0	5.171	11.949	0.273	0.265	0.035	98.272
MGC-4-1	48.644	0.011	1.681	0.071	31.832	1.846	0.013	1.281	10.703	0.309	0.192	0.108	96.692
MGC-4-2	49.386	0.079	2.855	0.037	27.381	1.103	0	4.196	11.652	0.417	0.267	0	97.373
MGC-4-3	48.126	0.034	3.153	0	31.828	1.184	0.017	1.671	10.916	0.395	0.194	0.12	97.637
Average	48.529	0.028	3.439	0.023	29.315	1.051	0.015	2.908	11.272	0.44	0.301	0.066	97.387

[a] MGC-5-1, MGC-5-2, *etc.* are from the same MGC-5 sample. Likewise, MGC-4-1, MGC-4-2, *etc.* are from the same MGC-4 sample.

CaO, FeO, and MgO, in addition to a small amount of Al$_2$O$_3$, MnO, Na$_2$O, and K$_2$O. The total amount of minerals in this assay is approximately 97%, and the remainder is assumed to be water because the anion content could not be monitored by EPMA. Results show that the average contents of SiO$_2$ and CaO are 48.529 and 11.272 wt%. The FeO content ranges from 23.485 to 31.832 wt%, which is considerably higher than that of actinolite, but approaching that of ferro-actinolite (29.4 wt%). The results revealed that these inclusions are Ca–Fe-rich amphiboles with compositions very close to the end-member ferro-actinolite.[13] The unit formula of amphiboles was calculated using the program AMFORM, as shown in Table 3.[33] After discarding unreliable EPMA data, the average chemical formulae of the amphibole inclusion in green rutilated quartz is $[Na_{0.04}K_{0.05}]_{0.09}[Ca_{1.89}Na_{0.11}]_2[Mg_{0.54}Fe_{3.74}^{2+}Fe_{0.28}^{3+}Mn_{0.15}Al_{0.28}]_{4.99}[Si_{7.47}Al_{0.53}]_8O_{22}(OH)_2$.

The amount and proportion of trace elements in amphiboles are affected by the composition of the melt at the time of formation and the output environment.[34] When amphiboles are present in the strong mineralization zone, the F and Cl content is higher while the weak mineralization zone has higher iron oxide content.[35] This suggests that the mineralizing elements in the strong mineralized zones are conducive to mineralization, while the iron elements in the weak mineralized zones are more in the form of oxides.

3.5. Name of amphibole inclusions

Amphibole is a double-chain silicate mineral with the chemical formula:[36]

$A_{0-1}B_2C_5^{VI}T_8^{IV}O_{22}(OH,F,Cl)_2$, where the Roman numerals in the upper corner indicate the coordination number and the Arabic numerals in the lower corner indicate the atomic number. A represents Na$^+$ and K$^+$ ions, which frequently occupy the A site. B represents Na$^+$, Li$^+$, K$^+$, Ca^{2+}, Mg^{2+}, Fe^{2+}, and Mn^{2+} ions, which frequently occupy the M$_4$ site. C represents Mg^{2+}, Fe^{2+}, Mn^{2+}, Al^{3+}, Fe^{3+}, Ti^{4+}, and Cr^{3+} ions, which frequently occupy the M$_1$, M$_2$, and M$_3$ sites, and T represents Si^{4+} and Al^{3+} in the four-coordination sites T$_1$ and T$_2$.

By determining the type of amphiboles, it is possible to infer the magmatic evolution process in the region, which in turn provides new evidence for the origins of mineral deposits.[37] The amphiboles are classified primarily into four groups depending on the occupancy of the B sites. There are four types of amphiboles as follows:

(1) Mg–Fe–Mn–Li group: when (Ca + Na)$_B$ < 1.00 and the sum of (Mg, Fe, Mn, Li)$_B$ ions ≥ 1.00. (2) Calcic group: (Ca + Na)$_B$ ≥ 1.00 while Na$_B$ < 0.50 usually Ca$_B$ ≥ 1.50. (3) Sodic-calcic group: (Ca + Na)$_B$ ≥ 1.00 while Na$_B$ is in the range of 0.50–1.50. (4) Sodic group: Na$_B$ ≥ 1.50. These groups are further subdivided with respect to Si and Mg/(Mg + Fe^{2+}) or Mg /(Mg + Mn^{2+}).

The chemical composition of the samples was characterized by rich Fe and Ca, poor Mg, Na and K, and Ca was ≥1.50, Na + K was ≤0.5. The inclusions were named according to the principles of naming amphibole by the Commission on Nomenclature of New Minerals and Minerals of the International Mineralogical Association. According to the principles of classification, it belonged to the calcic amphiboles. Based on the amphibole classification principles proposed by Leake *et al.*

Table 3 The unit formula of amphibole inclusions calculated by the program AMFORM

	MGC-5-1	MGC-5-2	MGC-5-3	MGC-5-4	MGC-5-5	MGC-5-6	MGC-5-7	MGC-5-8	MGC-1-1	MGC-2-1	MGC-4-1	MGC-4-2	MGC-4-3	Average
Si	7.308	7.805	7.706	7.692	7.684	7.704	7.425	7.694	7.551	7.797	7.837	7.742	7.63	7.66
Al^{IV}	0.692	0.195	0.294	0.308	0.316	0.296	0.575	0.306	0.449	0.203	0.163	0.258	0.37	0.34
Al^{VI}	0.348	0.34	0.306	0.395	0.268	0.42	0.322	0.289	0.37	0.182	0.156	0.269	0.22	0.299
Ti	0.002	0	0.005	0	0.008	0.001	0.002	0.002	0	0.009	0.001	0.009	0.004	0.003
Cr	0.007	0	0	0	0	0.008	0	0.001	0.008	0	0.009	0.005	0	0.003
Ni + Zn	0.01	0	0.002	0	0	0.005	0	0.005	0	0	0.002	0	0.002	0.002
Fe^{3+}	0.293	0	0	0	0	0.028	0.119	0	0.05	0	0.131	0	0.272	0.069
Mg	0.684	0.565	0.869	0.62	0.663	0.569	0.691	0.644	0.69	1.192	0.308	0.981	0.395	0.682
Fe^{2+}	3.522	3.925	3.662	3.905	3.883	3.853	3.799	3.958	3.745	3.482	4.158	3.59	3.948	3.802
Mn	0.134	0.17	0.156	0.079	0.178	0.115	0.067	0.101	0.137	0.135	0.252	0.146	0.159	0.141
Ca	1.903	1.903	1.903	1.903	1.903	1.903	1.903	1.903	1.903	1.903	1.903	1.903	1.903	1.903
Na_B	0.097	0.097	0.097	0.097	0.097	0.097	0.097	0.097	0.097	0.097	0.097	0.097	0.097	0.097
Na_A	0.076	0	0.043	0.051	0.062	0	0.124	0.091	0.062	0.061	0	0.084	0	0.05
K	0.061	0.059	0.056	0.093	0.067	0.049	0.076	0.083	0.059	0.052	0.039	0.053	0.039	0.061
OH	2	1.939	1.947	1.868	1.974	2	2	1.887	2	1.911	2	1.871	2	1.954
O	0	0.061	0.053	0.132	0.026	0	0	0.113	0	0.089	0	0.129	0	0.046

(1997) (Fig. 8),[36] the green amphibole inclusions can be named ferro-actinolite in the subclass of calcic amphiboles with a few named ferro-hornblende.

Calcic amphiboles can be further classified into alkaline and calc-alkaline amphiboles based on the K content.[38] The K content in calc-alkaline amphiboles is generally lower than alkaline amphiboles, and so the alkaline and calc-alkaline amphiboles can be determined using the K–Al diagram. As can be seen in Fig. 9, the amphibole inclusions of the samples are all calc-alkaline.

In summary, the green acicular inclusions in green rutilated quartz belong to calcic-alkaline amphiboles. Most of them are ferro-actinolite and a few are ferro-hornblende.

3.6. Mineralization process and coloring analysis

The determination of the amphibole genesis types helps to explain the genesis and the diagenesis of the different rock shells. According to previous studies, Si and Ti in amphiboles

can be used as a boundary to delineate the type of amphibole genesis.[39] Ma *et al.* (1994) combined Si and Ti contents to discriminate the type of amphibole genesis and divided the Si–Ti variogram of calcic amphiboles into five zones.[40] It was concluded that amphiboles associated with volcanic rocks are characterized by high Ti and low Si, whereas alteration, replacement or secondary amphiboles are characterized by low Ti and high Si. Ti and Si are relatively balanced in amphiboles associated with basic and intermediate-acid intrusive rocks. In this study, we analyzed the cast map in the amphibole genesis model provided by Ma *et al.* (1994) (Fig. 10), which showed that the green amphibole inclusions fell in region V. This area is a product of secondary alteration or metasomatism after consolidating the rocks. Theoretically, Fe-rich actinolite usually forms after magma consolidation.[41] Combined with the chemical compositional of Fe-rich characteristics of the amphibole inclusions, it suggests that the amphibole inclusions of the samples were formed by later alteration or metasomatism.
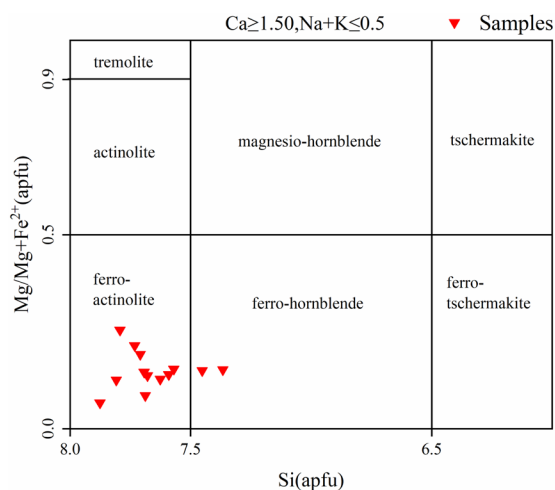

Fig. 8 Diagram of amphibole classification (adapted from Leake *et al.*, 1997 (ref. 36)) (apfu = atoms per formula unit).
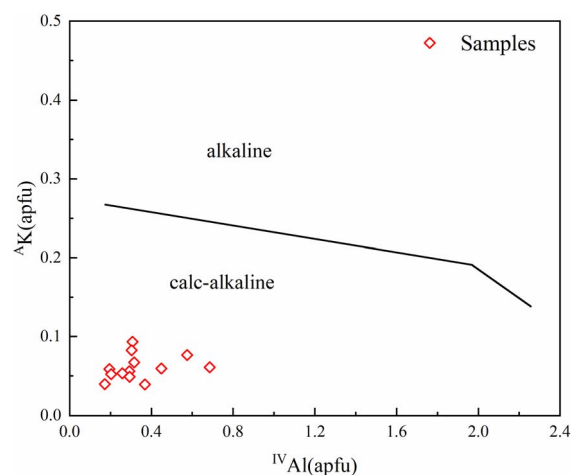

Fig. 9 The division of calc–alkaline and alkaline series in calcic amphiboles (adapted from Ridolfi, F. *et al.*, 2012 (ref. 38)) (apfu = atoms per formula unit).
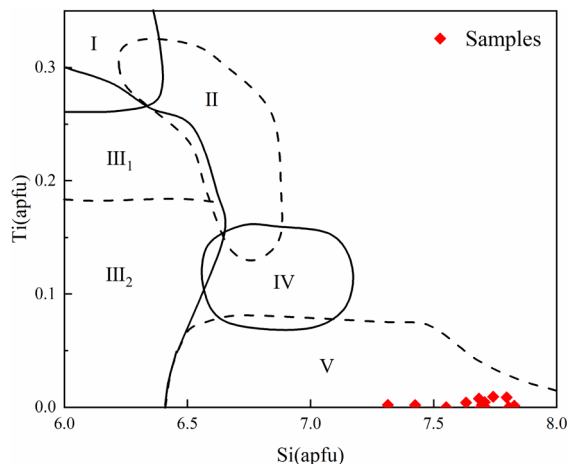
Fig. 10 Si–Ti variation figure for calcic amphiboles and genetic classification. (I: amphibole in volcanic rocks; II: amphibole in basal-ultramafic rocks; III: amphibole in (III₁ high-grade metamorphic/III₂ metamorphic) rocks; IV: amphibole in neutral acid intrusive rocks; V: amphibole in alteration or metasomatism rocks) (adapted from Ma *et al.*, 1994 (ref. 40)).

Based on the spatial, mineralogical, and symbiotic relationships between the veins in the Huanggangliang mine, the mineralization process can be divided into four stages. Stage I is known as the skarn stage, and the minerals present are mainly rutile, diopside, and garnet. A small amount of magnetite is produced during the later stages of this stage. Stage II is the degradation and alteration stage. The minerals present in this stage are mainly hornblende, actinolite, and chrysocolla. Amphibole is radiating and fibrous, usually coexisting with quartz, fluorite, and other vein minerals. In stage III, the mineral composition is primarily molybdenite and scheelite. Late-stage minerals such as quartz, carbonate, fluorite, and chlorite are found in crevices or in clustered crystals within the ore deposits. The fourth stage consists of fine veins of carbonate.[5,42,43] Reactivation of the K-feldspar granite magma formed pegmatite veins, fine-grained veins and feldspar–quartz–cassiterite veins near the rock mass. The magma and hydrothermal fluids exerted a strong influence on the skarn ore body, resulting in fluoritization, chloritization, silicification, and Sn–Fe mineralization. Owing to the complexity of the mineralizing environment and the composition of the mineralizing solution, the morphology of the green rutilated quartz samples from this production area is highly variable. The green acicular inclusions in the sample are ferro-actinolite, and there is no obvious directional distribution characteristic, and the formation temperature of ferro-actinolite is higher than that of quartz.[6,44,45] Therefore, it can be judged that the formation time of ferro-actinolite inclusions is earlier than that of crystals. In the late stage of ferro-actinolite crystallization, under the force of mineralizing hydrothermal fluid, the underdeveloped ferro-actinolite migrated around with the power. When migrating to the vicinity of the quartz, with the gradual decrease of temperature, the ferro-actinolite is trapped inside the crystal and forms a green rutilated quartz.

Rutilated quartz from Inner Mongolia appears green, which is actually due to a large number of internal green actinolite inclusions. Similarly, the fluorite and gray crystals produced there are also due to a large number of internal inclusions that mask their own color.[46]

4 Conclusions

In summary, the green rutilated quartz from Inner Mongolia appears dark green due to the large number of actinolite inclusions in it. It belongs to the allochromatic color. Inclusions are light green and along the hairline extension direction and appear as obvious longitudinal lines. The morphology of the inclusions is not regular. They always show a random arrangement, morphologically fibrous, acicular, *etc.* The overall display has more tops and fewer bottoms, more surfaces, and fewer interiors. The composition of the inclusions was calculated to be ferro-actinolite in the subclass of calcic-alkaline amphibole, with a few calculated to be ferro-hornblende. Based on the relationship between the chemical composition and genesis of the amphibole inclusions, it is considered that the green inclusions in the quartz were formed by secondary alteration or metasomatism processes. Under the dynamic action of the multi-stage metallogenic hydrothermal fluid in the late stage of mineralization, actinolite migrated. Moreover, with the rapid decrease of temperature, crystals wrapped with a large number of acicular inclusions were crystallized. This study brings new data for the gemological characterization and acicular inclusions of green rutilated quartz in Huanggangliang, Inner Mongolia.

Author contributions

Shuxin Zhao and Tao Li: data collection, writing – original draft; Qingfeng Guo: analysis, review and editing, supervision; Liangyu Liu: software; Yinghua Rao: investigation; Libing Liao: data curation; All authors have read and approved the final manuscript.

Conflicts of interest

The authors declare that they have no known competing financial interests or personal relationships that could have appeared to influence the work reported in this paper.

Acknowledgements

References

1 J. S. Goreva, C. Ma and G. R. Rossman, Fibrous nanoinclusions in massive rose quartz: the origin of rose

coloration, *Am. Mineral.*, 2001, **86**(4), 466–472, DOI: **10.2138/am-2001-0410**.

2 A. K. Sandhu and O. P. Pandey, FTIR and TL studies of gamma rays irradiated natural quartz, *J. Mater. Sci.: Mater. Electron.*, 2021, **32**(15), 20767–20776, DOI: **10.1007/s10854-021-06590-2**.

3 L. Leon-Reina, J. M. Compana, A. G. De la Torre, R. Moreno, L. E. Ochando and M. A. G. Aranda, Powder diffraction analysis of gemstone inclusions, *Powder Diffr.*, 2011, **26**(1), 48–52, DOI: **10.1154/1.3552672**.

4 J. Dong, L. B. Jia, S. M. Jia, *et al.*, Trace element signature of hydrothermal quartz: a potential tracer for ore genesis, *Arabian J. Geosci.*, 2022, **15**(24), 1768, DOI: **10.1007/s12517-022-11070-w**.

5 Y. Li, Z. Liu, Y. Shao, *et al.*, Genesis of the Huanggangliang Fe-Sn polymetallic deposit in the southern Da Hinggan Range, NE China: constraints from geochronology and cassiterite trace element geochemistry, *Ore Geol. Rev.*, 2022, **151**, 105226, DOI: **10.1016/j.oregeorev.2022.105226**.

6 E. Fritsch, Hematite Inclusions in Red Trapiche Quartz from Inner Mongolia, *J. Gemmol.*, 2021, **37**(6), 569–571, DOI: **10.15506/JoG.2021.37.6.569**.

7 K. Sato and M. Santosh, Titanium in quartz as a record of ultrahigh-temperature metamorphism: the granulites of Karur, southern India, *Mineral. Mag.*, 2007, **71**(2), 143–154, DOI: **10.1180/minmag.2007.071.2.143**.

8 V. Maneta and P. Voudouris, Quartz Megacrysts in Greece: Mineralogy and Environment of Formation, *Bull. Geol. Soc. Greece*, 2010, **43**(2), 685–696, DOI: **10.12681/bgsg.11231**.

9 X. F. Li, Z. Y. Chen, R. C. Wang, J. Xu, P. A. Wang and J. J. Yu, Mineralogical and geochemical features of hair-like rutile in rocked quartz in Donghai, Jiangsu Province, China, *Acta Pet. Sin.*, 2005, **21**(2), 475–481.

10 L. Faber, Glass Doublets Simulating Rutilated and Tourmalinated Quartz, *J. Gemmol.*, 2018, **36**(1), 20–21.

11 A. Muller, B. J. Williamson and M. Smith, Origin of quartz cores in tourmaline from Roche Rock, SW England, *Mineral. Mag.*, 2005, **69**(4), 381–401, DOI: **10.1180/0026461056940258**.

12 A. Kassolifournaraki and K. Michailidis, Chemical-Composition of Tourmaline in Quartz Veins from Nea-Roda and Thasos Areas in Macedonia, Northern Greece, *Can. Mineral.*, 1994, **32**, 607–615, ISSN:0008-4476.

13 S. Klemme, J. Berndt, C. Mavrogonatos, *et al.*, On the Color and Genesis of Prase (Green Quartz) and Amethyst from the Island of Serifos, Cyclades, Greece, *Minerals*, 2018, **8**(11), 487, DOI: **10.3390/min8110487**.

14 G. Lehmann and H. U. Bambauer, Quarzkristalle und ihre Farben, *Angew. Chem.*, 1973, **85**(7), 281–289, DOI: **10.1002/ange.19730850703**.

15 G. Lehmann, Yellow color centers in natural and synthetic quartz, *Phys. Kondens. Mater.*, 1971, **13**(4), 297–306, DOI: **10.1007/BF02422610**.

16 M. Czaja, M. Kądziołka-Gaweł, A. Konefał, *et al.*, The Mössbauer spectra of prasiolite and amethyst crystals from Poland, *Phys. Chem. Miner.*, 2017, **44**(5), 365–375, DOI: **10.1007/s00269-016-0864-z**.

17 G. R. Rossman, Colored varieties of the silica minerals, *Rev. Mineral. Geochem.*, 1994, **29**(1), 433–467, corpus ID: 93142580.

18 L. Jiang, Z. Chen and Y. Liu, The Chemical Composition of Trapiche-like Quartz from Huanggangliang Area, Inner Mongolia, China, *Crystals*, 2022, **12**(1), 122, DOI: **10.3390/cryst12010122**.

19 A. Kröner, E. Hegner, B. Lehmann, *et al.*, Palaeozoic arc magmatism in the Central Asian Orogenic Belt of Kazakhstan: SHRIMP zircon ages and whole-rock Nd isotopic systematics, *J. Asian Earth Sci.*, 2008, **32**(2), 118–130, DOI: **10.1016/j.jseaes.2007.10.013**.

20 B. M. Jahn, The central Asian orogenic belt and growth of the continental crust in the phanerozoic, in *Workshop on Tectonic Processes in the Evolution of China*, Univ Hong Kong, Dept. Earth Sci., Hong Kong, P. R. China, 2004, vol. 226, pp. 73–100, DOI: **10.1144/gsl.Sp.2004.226.01.05**.

21 C. A. Trepmann and B. Stöckhert, Short-wavelength undulatory extinction in quartz recording coseismic deformation in the middle crust – an experimental study, *Solid Earth*, 2013, **4**(2), 263–276, DOI: **10.5194/se-4-263-2013**.

22 G. West, A Note on Undulatory Extinction of Quartz in Granite, *Q. J. Eng. Geol.*, 1991, **24**(1), 159–165, DOI: **10.1144/GSL.QJEG.1991.024.01.16**.

23 B. Lafuente, R. T. Downs, H. Yang and N. Stone, The power of databases: the RRUFF project, in *Highlights in Mineralogical Crystallography*, ed. T. Armbruster and R. M. Danisi, W. De Gruyter, Berlin, Germany, 2015, pp. 1–30, **https://rruff.info/about/downloads/HMC1-30.pdf**.

24 D. G. Alkmim, F. O. T. D. Almeida and F. S. Lameiras, FTIR study of aquamarines after gamma irradiation, heat treatment and electrodiffusion, *REM*, 2017, **70**(3), 289–292, DOI: **10.1590/0370-44672016700076**.

25 J. C. Pei, L. W. Fan and H. Xie, Study on the Vibrational Spectra and XRD Characters of Huanglong Jade from Longling County, Yunnan Province, *Spectrosc. Spectral Anal.*, 2014, **34**(12), 3411–3414, DOI: **10.3964/j.issn.1000-0593(2014)12-3411-04**.

26 A. K. Sandhu and O. P. Pandey, FTIR and TL studies of gamma rays irradiated natural quartz, *J. Mater. Sci.: Mater. Electron.*, 2021, **32**(15), 20767–20776, DOI: **10.1007/s10854-021-06590-2**.

27 B. J. Saikia, G. Parthasarathy and N. C. Sarmah, Fourier transform infrared spectroscopic estimation of crystallinity in SiO_2 based rocks, *Bull. Mater. Sci.*, 2008, **31**(5), 775–779, DOI: **10.1007/s12034-008-0123-0**.

28 B. W. Evans and H. Yang, Fe-Mg order-disorder in tremolite-actinolite-ferro-actinolite at ambient and high temperature, *Am. Mineral.*, 1998, **83**(5–6), 458–475, DOI: **10.2138/am-1998-5-606**.

29 J. Fukuda and K. Shinoda, Water molecules in beryl and cordierite: high-temperature vibrational behavior, dehydration, and coordination to cations, *Phys. Chem. Miner.*, 2011, **38**(6), 469–481, DOI: **10.1007/s00269-011-0420-9**.

30 K. Li and X. Shen, Research on Identification Characteristics of Tremolite and Actinolite by Using Nondestructive Testing

Techniques of Infrared Spectroscopy and Raman Spectroscopy, *Bull. Mineral. Petrol. Geochemistry*, 2019, **38**(2), 405–408, DOI: 10.19658/j.issn.1007-2802.2019.38.036.

31 N. Bolfan-Casanova, G. Montagnac and B. Reynard, Measurement of water contents in olivine using Raman spectroscopy, *Am. Mineral.*, 2014, **99**(1), 149–156, DOI: 10.2138/am.2014.4444.

32 Y. Qin, G. Song, Y. Lv, W. Chen and Y. Hu, Application of EPMA in microstructures and composition analysis of Cladosiphonia fossils, *Acta Micropalaeontol. Sin.*, 2022, **39**(4), 361–372.

33 F. Ridolfi, A. Zanetti, A. Renzulli, D. Perugini, F. Holtz and R. Oberti, AMFORM, a new mass-based model for the calculation of the unit formula of amphiboles from electron microprobe analyses, *Am. Mineral.*, 2018, **103**(7), 1112–1125, DOI: 10.2138/am-2018-6385.

34 R. Shinjo and Y. Kato, Geochemical constraints on the origin of bimodal magmatism at the Okinawa Trough, an incipient back-arc basin, *Lithos*, 2000, **54**(3–4), 117–137, DOI: 10.1016/S0024-4937(00)00034-7.

35 Z. Chen, Z. Zeng, X. Wang, X. Yin, S. Chen, X. Li and H. Qi, Geochemical characteristics of amphiboles in the rhyolite from the southern Okinawa Trough, and its implication for petrogenesis, *Acta Oceanol. Sin.*, 2017, **39**(12), 74–89.

36 B. E. Leake, A. R. Woolley, W. D. Birch, *et al.*, Nomenclature of amphiboles – report of the subcommittee on amphiboles of the International Mineralogical Association Commission on New Minerals and Mineral Names, *Eur. J. Mineral.*, 1997, **9**(3), 623–651, DOI: 10.1127/ejm/9/3/0623.

37 X. Cui, S. Su, W. Meng, L. Liu and C. Chen, The mineralogical characteristics of amphiboles in monzonite porphyry from the Wuan area, Hebei Province and their indications for the genesis of the skarn iron deposit, *Acta Pet. Sin.*, 2020, **36**(7), 2215–2231, DOI: 10.18654/1000-0569/2020.07.19.

38 F. Ridolfi and A. Renzulli, Calcic amphiboles in calc-alkaline and alkaline magmas: thermobarometric and chemometric empirical equations valid up to 1130 °C and 2.2 GPa, *Contrib. Mineral. Petrol.*, 2012, **163**(5), 877–895, DOI: 10.1007/s00410-011-0704-6.

39 A. R. Chivas, Geochemical evidence for magmatic fluids in porphyry copper mineralization: part I. Mafic silicates from the koloula igneous complex, *Contrib. Mineral. Petrol.*, 1982, **78**(4), 389–403, DOI: 10.1007/BF00375201.

40 C. Q. Ma, K. G. Yang and Z. H. Tang, *et al.*, *Magma-dynamics of Granitoids Theory, Method and a Case Study of the Eastern Hubei Granitoids*, China University of Geosciences Press, Wuhan, 1994, ISBN:7-5625-0930-1.

41 H. L. Lledo and D. M. Jenkins, Experimental Investigation of the Upper Thermal Stability of Mg-rich Actinolite; Implications for Kiruna-Type Iron Deposits, *J. Petrol.*, 2008, **49**(2), 225–238, DOI: 10.1093/petrology/egm078.

42 C. Wang, Y. Shao, X. Zhang, J. Dick and Z. Liu, Trace Element Geochemistry of Magnetite: Implications for Ore Genesis of the Huanggangliang Sn-Fe Deposit, Inner Mongolia, Northeastern China, *Minerals*, 2018, **8**(5), 195, DOI: 10.3390/min8050195.

43 W. Lijuan, W. Jingbin, W. Yuwang and M. Qian, Fluid-melt Inclusions in Fluorite of the Huanggangliang Skarn Iron-Tin Deposit and Their Significance to Mineralization, *Acta Geol. Sin. (Engl. Ed.)*, 2010, **75**(2), 204–211, DOI: 10.1111/j.1755-6724.2001.tb00522.x.

44 L. Li, D. Xu, Q. Huang, G. Chi, Z. Wang and K. Xu, Study on Ore-forming Fluid Source and Metallogenic Mechanism of the Gaotongling Quartz Vein Type Mo Deposit, Hainan Province, *Geotecton. Metallog.*, 2023, **47**(4), 778–790.

45 Y. Tang, J. Zhang, L. Fan, C. Qin, Y. Jin and F. Bai, Constraints of the magmatic evolution on the mineralization of Han-Xing type iron deposit: evidences from amphibole chemical compositions, *Acta Mineral. Sin.*, 2023, **43**(2), 215–224.

46 Y. Chen, Y. Han, B. Xu and J. Liu, Geochemical characteristics and genesis of red fluorite in the Huanggangliang Fe-Sn deposit, Inner Mongolia, *Acta Pet. Sin.*, 2021, **37**(12), 3869–3879, DOI: 10.18654/1000-0569/2021.12.15.